Journal of Fluids and Structures (1997) **11,** 909–928

SIMULATION OF TUBE BUNDLE VIBRATIONS INDUCED BY CROSS-FLOW

V. KASSERA

AEA Technology GmbH, D72108 Rottenburg, Germany

AND

K. STROHMEIER

Institute for Apparatus Engineering and Plant Design, Technical University of Munich, Germany

(Received 21 August 1996 and in revised form 10 September 1997)

A two-dimensional simulation model for flow-induced vibrations of tube bundles subjected to single-phase cross-flow is applied on six different bundles at realistic Reynolds numbers. The calculation scheme solves the unsteady Navier–Stokes equations, including turbulence modelling. Fluid forces, tube acceleration, tube velocity and tube displacements are computed after each time step due to the current flow field. The bundles are square and 30°-arrangements, with pitch-to-diameter ratios of 1·2 up to 2·4. The point of resonance or instability is determined by increasing the approach velocity step by step. The results are analysed and compared with experimental data and with design criteria proposed in the literature.

1. INTRODUCTION

FLOW-INDUCED VIBRATIONS of tube bundles in cross-flow has been the subject of a large number of investigations during the last 25 years. Several analytical criteria for the prediction of the instability threshold of tube bundles subjected to cross-flow were developed. An overview of this part of the research is given by Price (1995). Due to the rapidly increasing computer power, some CFD approaches have also appeared in the past. Ichioka *et al.* (1995), Sadaoka & Umegaki (1995) and Kassera *et al.* (1995), for example, presented such simulations. In each of these papers, the vibration of one tube bundle was investigated numerically. The advantages of this kind of solution are as follows.

(i) Compared with the conservative semi-empirical formulae for the prediction of the critical dimensionless velocity, a numerical approach has the potential of being more exact and can be used for arbitrary tube arrangements (for example, irregular arrangements are possible too). In addition, for any sub-critical velocity a prediction of tube amplitudes is possible.

(ii) The flow field can be visualized, and flow data (velocity and pressure field) and dynamical tube data (displacements and velocities of all tubes) are available at each time step. Furthermore, the influence of boundary conditions, such as wall friction or pump vibrations, can be investigated. From a scientific point of view this is very important,

0889–9746/97/080909 + 20 $25.00/fl970114

because the formation of unstable tube vibrations can be investigated by using a numerical simulation code as a tool.

The most important disadvantage of a simulation is the immense consumption of computation time, even on super-computers such as the CRAY YMP.

In this paper, a two-dimensional simulation model for flow-induced vibrations of tube bundles is used. The model solves the unsteady flow field and computes the fluid loads on each tube at every time step. Due to these forces the tubes can move in two directions independently of each other. All calculations presented here were carried out with the properties of water to make the results comparable with experimental data produced in a water tunnel. In contrast to the investigations of Ichioka *et al.* (1995) and Sadaoka & Umegaki (1995), a two-equation turbulence model is used; therefore, realistic Reynolds numbers up to Re = 200 000 can be calculated for the first time.

2. NUMERICAL FORMULATION

2.1. Determination of the Flow Field

The numerical formulation used in a former investigation (Kassera *et al.* 1995) was changed by the implementation of the k–ω turbulence model (Wilcox 1994). The main advantage, compared to Large-Eddy-Simulation (LES) used previously, is the absence of constants which have to be adjusted for each calculation. Furthermore, the model can easily be integrated through the viscous sub-layer and no wall functions need to be applied. Therefore, the governing equations in primitive variables for Cartesian coordinates can be written as (Patankar 1980)

$$\frac{\partial u}{\partial t} + u\frac{\partial u}{\partial x} + v\frac{\partial u}{\partial y} = -\frac{1}{\rho}\frac{\partial p}{\partial x} + \nu\left(\frac{\partial^2 u}{\partial x^2} + \frac{\partial^2 u}{\partial y^2}\right), \tag{1}$$

$$\frac{\partial v}{\partial t} + u\frac{\partial v}{\partial x} + v\frac{\partial v}{\partial y} = -\frac{1}{\rho}\frac{\partial p}{\partial y} + \nu\left(\frac{\partial^2 v}{\partial x^2} + \frac{\partial^2 v}{\partial y^2}\right), \tag{2}$$

$$\frac{\partial u}{\partial x} + \frac{\partial v}{\partial y} = 0. \tag{3}$$

The total viscosity ν, which is not identical with the viscosity of the flow medium ν_f, is calculated by

$$\begin{aligned} \nu &= \nu_f + \nu_t, \\ \nu_t &= k/\omega. \end{aligned} \tag{4}$$

For the turbulence quantities k and ω, two additional transport equations must be solved:

$$\frac{\partial k}{dt} + u\frac{\partial k}{\partial x} + v\frac{\partial k}{\partial y} = T - \beta^* k\omega + \frac{\partial}{\partial x}\left[(\nu + \sigma^*\nu_t)\frac{\partial k}{\partial x}\right] + \frac{\partial}{\partial y}\left[(\nu + \sigma^*\nu_t)\frac{\partial k}{\partial y}\right], \tag{5}$$

$$\frac{\partial \omega}{\partial t} + u\frac{\partial \omega}{\partial x} + v\frac{\partial \omega}{\partial y} = \alpha\frac{\omega}{k}T - \beta\omega^2 + \frac{\partial}{\partial x}\left[(\nu + \sigma\nu_t)\frac{\partial \omega}{\partial x}\right] + \frac{\partial}{\partial y}\left[(\nu + \sigma\nu_t)\frac{\partial \omega}{\partial y}\right], \tag{6}$$

with

$$\frac{T}{v_t} = 2\left(\frac{\partial u}{\partial x}\right)^2 + \left(\frac{\partial v}{\partial x}\right)^2 + \left(\frac{\partial u}{\partial y}\right)^2 + 2\left(\frac{\partial v}{\partial y}\right)^2 + 2\frac{\partial v}{\partial x}\frac{\partial u}{\partial y}, \tag{7}$$

and the closure coefficients

$$\alpha = \tfrac{5}{9}, \quad \beta = \tfrac{3}{40}, \quad \beta^* = \tfrac{9}{100}, \quad \sigma = \tfrac{1}{2}, \quad \sigma^* = \tfrac{1}{2}.$$

It is important to note that the closure coefficients are valid for all flow cases. Wilcox (1994) reports in detail how they were obtained.

The set of equations is solved by the Finite Volume Method. The diffusive fluxes are discretized by central differences, convective fluxes by the QUICK-scheme (Leonard 1979). Discretization of time is done implicitly.

The linearized differential equations are decoupled by the SIMPLE-algorithm (Patankar 1980) and solved by the Gauss–Seidel point-by-point iteration method. With these algorithms a very well vectorizable code can be obtained.

2.2. Computation of Tube Motion

For calculating the flow-induced motion, the tubes are treated as rigid cylinders, which are supported by linear-elastic springs. Therefore, the equations for acceleration, velocity and displacement — for example in the y-direction — can be written as

$$\ddot{y}^{t^0+\Delta t} = \frac{F_y^{t^0+\Delta t} - c\Delta y^{t^0}}{m_s + m_c} - 4\pi\zeta f_n \dot{y}^{t^0}, \tag{8}$$

$$\dot{y}^{t^0+\Delta t} = \dot{y}^{t^0} + \ddot{y}^{t^0+\Delta t}\Delta t, \tag{9}$$

$$\Delta y^{t^0+\Delta t} = \Delta y^{t^0} + (\dot{y}^{t^0+\Delta t} + \dot{y}^{t^0})\frac{\Delta t}{2} + \ddot{y}^{t^0+\Delta t}\frac{\Delta t^2}{2}. \tag{10}$$

The superscript t^0 denotes that the quantity was calculated at the end of the previous time step, while $t^0 + \Delta t$ corresponds to values at the end of the present time step. It is important to note that the damping factor ζ represents only structural damping. F_y is the sum of all fluid forces in the y-direction and is determined by solving the flow field. It contains all excitation forces and the fluid damping force. Therefore, an explicit value for the fluid damping is not given by the calculation. However, the advantage of this kind of solution is the fact that the calculation can be carried out without any knowledge of the uncertain fluid damping value, because this is not an input parameter.

Tube motion in the grid is realized by using a sub-grid for each tube, as presented in Figure 1. Within these tube grids, cells can be expanded or compressed; therefore, the tubes are able to move in two directions (Figure 2). The field variables from the previous time step are interpolated to the new grid locations by a four-point linear interpolation algorithm. Because the tube displacement per time step is small, this method provides sufficient accuracy. All tube grids are connected to a base grid, which is used for calculating the approaching flow and the wake behind the bundle. Additionally, the base grid represents the flow channel.

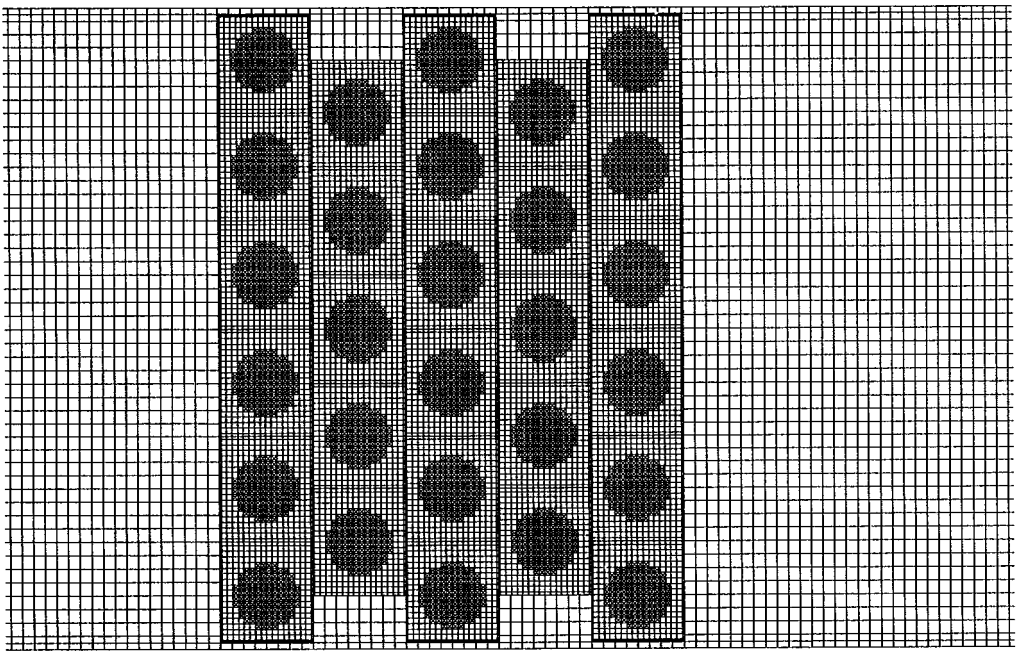

Figure 1. Grid without tube displacements.

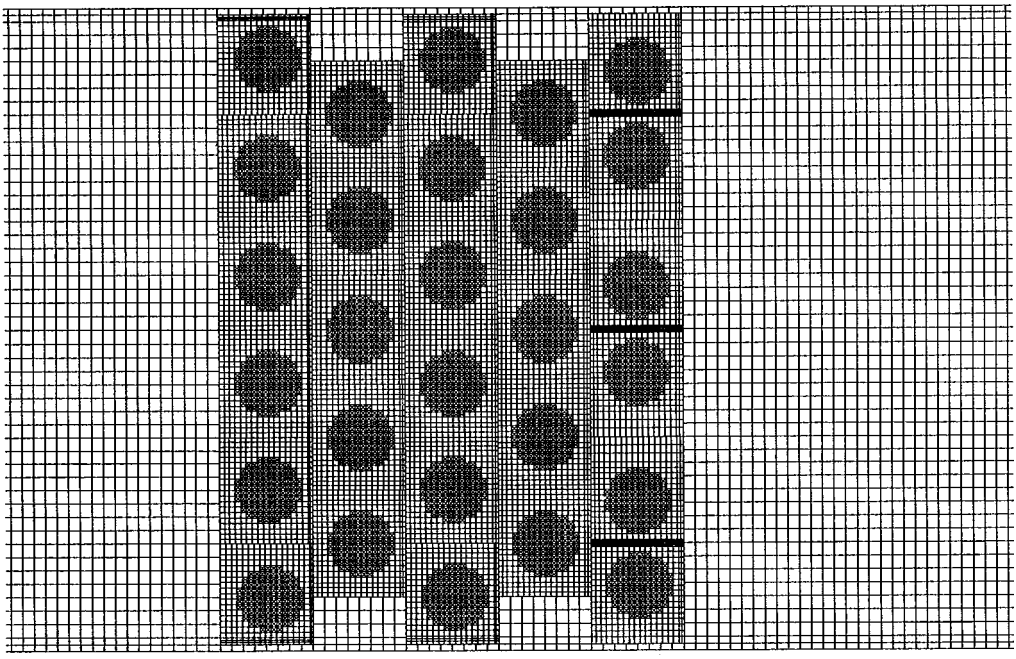

Figure 2. Grid with displaced tubes.

2.3. Flow-Field/Tube–Motion Coupling

To calculate the flow-induced vibrations of the tubes, the following procedure is followed at each time step.

(a) Calculation of the flow field at $t = t^0 + \Delta t$ with the boundary conditions of $t = t^0$.

(b) Determination of lift and drag loads.

(c) Computation of tube velocities $\dot{x}$ and $\dot{y}$ and the tube displacements Δx and Δy [equations (9) and (10)].

(d) Regeneration of the grid around each tube due to the current tube displacements Δx and Δy.

(e) The tube velocities $\dot{x}$ and $\dot{y}$ form the boundary conditions for the next time step. Therefore, at the tube surfaces the following assignment is made:

$$u = \dot{x}, \quad v = \dot{y}. \tag{11}$$

Then the calculation can proceed with step (a) again.

3. EXPERIMENTAL SET-UP

The experimental set-up is described in detail in Kassera & Strohmeier (1994). All experiments were conducted in a water tunnel with a rectangular measurement section (Figure 3). The approaching flow is uniform over the length of the tubes. The tested tube bundles consist of 4×4 up to 8×8 tubes, with one fixed and one free end. Till today, over 100 configurations with pitch-to-diameter ratios of 1·2 up to 2·4 were tested. In each bundle, three measuring tubes were installed, using wire-strain gauges to measure the in-line and the

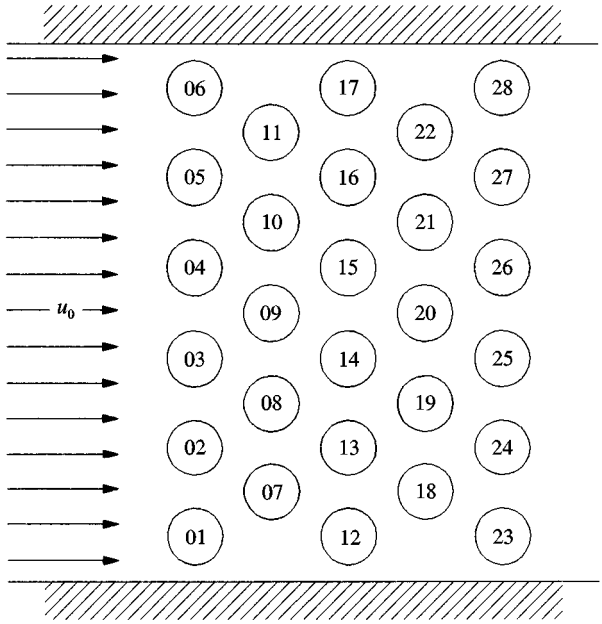

Figure 3. Test configuration (here bundle 14 is shown).

TABLE 1
Simulated tube bundles

Bundle	03	12	05	14	07	16
P/D	2·4	2·4	1·6	1·6	1·2	1.2
Material	Steel	Steel	Alu	Steel	Alu	Alu
D (mm)	8·0	8·0	12·0	12·0	16·0	16·0
Arrangement	90°	30°	90°	30°	90°	30°
m_s (kg/m)	0·174	0·174	0·093	0·273	0·127	0·127
m_c (kg/m)	0·028	0·028	0·079	0·079	0·154	0·154
m_a (kg/m)	0·054	0·054	0·144	0·144	0·351	0·351
ζ	—	—	0·0161	0·0150	0·0145	0·0145
δ_r	—	—	0·222	0·324	0·225	0.225
f_n (Hz)	23.8	23.8	24.2	33.4	27.2	27.2
$u_{0,\mathrm{crit,th}}$ (m/s)	—	—	0·15	0·26	0·10	0·10
$u_{0,\mathrm{crit,exp}}$ (m/s)	—	—	0·35	0·57	0·20	0·23
$u_{r,\mathrm{crit,exp}}$	—	—	3·23	3·79	2·76	3·18

cross-stream motion of the tube. Each bundle was tested by increasing the velocity by 12 equidistant steps. To ensure reproducibility, this procedure was repeated three times. Those bundles which were investigated numerically are shown in Table 1, together with all relevant dynamical data.* The added mass m_a was calculated as suggested by Blevins (1990):

$$m_a = \frac{\rho D^2 \pi}{4}\left[\frac{(D_e/D)^2 + 1}{(D_e/D)^2 - 1}\right], \tag{12}$$

with

$$D_e/D = (1 + 0{\cdot}5P/D)P/D. \tag{13}$$

To get data which are consistent with the database presented by Pettigrew & Taylor (1991), the damping factor was obtained by free-oscillation tests with single tubes in water. Therefore, it includes fluid damping. The theoretical critical approach velocity $u_{0,\mathrm{crit,th}}$ was determined by the criterion

$$u_{r,\mathrm{crit,th}} = \frac{u_{0,\mathrm{crit,th}}}{f_n D} = 3{\cdot}0\delta_r^{0{\cdot}5}. \tag{14}$$

With the critical approach velocity observed in the experiments $u_{0,\mathrm{crit,exp}}$, the reduced critical velocity is defined as

$$u_{r.\mathrm{crit,exp}} = \frac{u_{0,\mathrm{crit,exp}}}{f_n D}. \tag{15}$$

Therefore, the experimental results presented here can be compared with the data given for 90°- and 30°-arrangements in Pettigrew & Taylor (1991). Figure 4 shows that the

* The bundles 03 and 12 have a pitch-to-diameter ratio of $P/D = 2{\cdot}4$. In this case, vortex-induced vibrations are dominant. Therefore, the parameters for calculating the fluid elastic instability threshold are not given in Table 1.

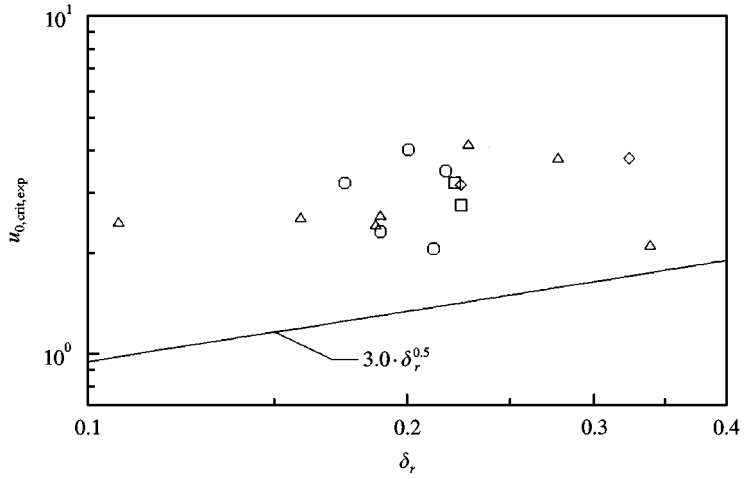

Figure 4. Comparison of experimental data: △, Pettigrew & Taylor (1991) for squares in-line array (90°); ○, Pettigrew & Taylor for staggered array (30°); □, Kassera & Strohmeier (1994) for square in-line array (90°); ◇, Kassera & Strohmeier (1994) for staggered array (30°).

experimental data correspond well with the data from the literature. The advantages of the data presented here are: (i) based on certain and well-known test conditions, a broad range of parameters is covered; and (ii) for all bundles the sub-critical amplitudes were measured. Especially, the second point is very important for comparisons with data obtained numerically.

4. RESULTS

4.1. Test Calculations

Before using the calculation code for the simulation of tube-bundle vibrations, a lot of test computations were conducted to obtain an optimal grid spacing, to proof the turbulence model and to adjust numerical parameters like the time increment Δt or the maximum number of iteration sweeps per time step n_{it}. A credible simulation result should be independent of these numerical quantities. Theoretically, this can be obtained easily by choosing very small grid spacing, short time steps and many iteration sweeps. In practice, however, this method would require too much computation time. Therefore, the goal of the test calculations was to obtain default values for these parameters, which are a compromise between result accuracy and computation cost. The grid depicted in Figure 1 with only one fixed tube in the middle of the computational domain was used for this purpose. Grid spacing of all cells was the same as in Figure 1. The only difference was that the cells normally representing the tubes were fluid volumes, with the exception of one tube in the middle of the channel.

To check the turbulence model, Re = 140 000 was chosen, because detailed experimental data exists for that case (Cantwell & Coles 1983). After an extensive test-series, a standard adjustment of the numerical parameters was obtained, which was used in all further calculations described in this paper. Table 2 shows the influence of the most important parameters on two test results, the mean drag coefficient C_d and the Strouhal number St. To

TABLE 2
Variation of numerical parameters

Modified parameter			C_d	St
Δx_{bg}: ± 00·0%	Δx_{tg}: + 33·3%		− 19·7%	+ 10·5%
Δx_{bg}: − 25·0%	Δx_{tg}: ± 00·0%		+ 2·7%	+ 2·1%
Δx_{bg}: − 25·0%	Δx_{tg}: − 33·3%		+ 4·7%	+ 4·2%
Δt: − 40·0%			+ 0·8%	+ 3·0%
n_{it}: + 50·0%			+ 0·8%	+ 0·1%

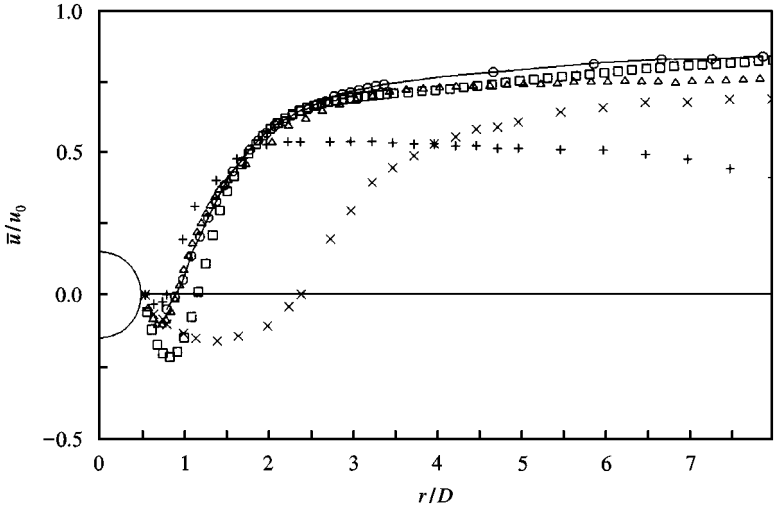

Figure 5. Mean velocities in the wake of a single fixed tube for Re = 140 000: ○, experimental data by Cantwell & Coles (1983); ×, numerical data by Franke (1991) using k–ε turbulence model; +, numerical data by Franke (1991) using LRR Reynolds stress turbulence model; △, numerical data by Kassera *et al.* (1995) using LES; □, numerical data presented here using k–ω turbulence model.

get these values, Δx_{bg}, Δx_{tg}, Δt and n_{it} were modified starting with the standard adjustment in each case. It can be seen that increasing the spacing of the tube grids by 33% changes the computed drag coefficient and Strouhal number significantly. However, refining the base grid by 25% and the tube grids by 33% simultanously leads only to minor changes of these computation results. Decreasing the time-step size or increasing the number of maximum iteration sweeps also changes the quantities C_d and St only by a small amount.

To validate the turbulence model, the mean streamwise velocity component on the centreline behind the tube and the pressure coefficient around the tube surface was computed and compared with (a) experimental data of Cantwell & Coles (1983); (b) Franke's (1991) simulation data; he investigated several turbulence models using a polar grid: a low-Reynolds-number k–ε model and the Launder–Reece–Rodi differential stress (LRR) models; and (c) simulation data produced by the calculation scheme presented here, but using Large-Eddy-Simulation with Smagorinsky's sub-grid-scale eddy viscosity model (Kassera *et al.* 1995).

Figure 5 shows that the k–ε-based model fails completely in predicting the wake behind a tube at high Reynolds numbers. The best result in this comparison was obtained by using

the LES. However, the disadvantage of this kind of solution is the necessity of adjusting the Smagorinsky constant C_s, an empirical parameter which differs from flow-case to flow-case. Adjusting C_s properly costs an immense amount of computation time, because a lot of variations are required. With the LRR model, very good results are obtained in the near wake, but the prediction of the far wake is not satisfactory. In addition, Franke (1991) reports serious stability problems and high requirements in computing power when using the LRR model. The k–ω model, however, needs even less computation time than k–ε due to the absence of wall functions, and numerical stability is very satisfactory. The results in the far wake are very good, and the discrepancy in the near wake can be explained by the fact that the k–ω model is based on the Boussinesq approximation, which is inaccurate for flows over curved surfaces. For calculating the tube-bundle vibrations, however, it is not important to predict secondary motions in the flow channel, second-order details of the wake or to resolve the separation zone exactly; it is rather sufficient to get the correct Strouhal number and fluid forces and to predict the flow field behind a tube approximately.

Figure 6 depicts the time-averaged pressure coefficient on the cylinder surface. Again, the simulation with the k–ω model corresponds quite well with the experimental data, a presupposition for computing fluid forces. Concerning the use of a Cartesian grid, Figures 5 and 6 show that the results obtained by Franke's simulations on a polar grid are in the same range of accuracy. In this context, the only obvious weakness due to the straircase boundary of the cylinder is the scattering of the pressure coefficient near the point of separation at an angle of 65°. Because a polar grid cannot be used for representing a bundle of moving tubes in a rectangular channel, only a general body-fitted grid would be an alternative. Compared with rectangular grids, however, a considerable additional consumption of computation time and memory is necessary to perform the simulation due to additional terms in the transport equations. Because it seems that the turbulence model influences the results much

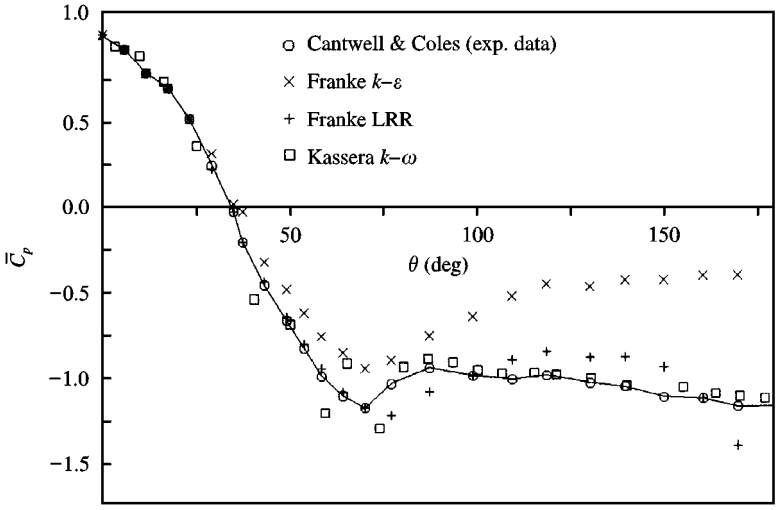

Figure 6. Pressure coefficient on the tube surface for Re = 140 000; ○, experimental data by Cantwell & Coles (1983); ×, numerical data by Franke (1991) using k–ε turbulence model; +, numerical data by Franke (1991) using LRR Reynolds stress turbulence model; □, numerical data presented here using k–ω turbulence model.

more than the different grids, and computation time is a very critical parameter for this kind of simulation, the use of the rectangular grid is appropriate in this case.

To test the calculation scheme over a wide range of Reynolds numbers, further computations were done. The correspondence with experimental data looks quite good. Figure 7 shows the predicted Strouhal number and Figure 8 the drag coefficient versus the Reynolds number. Again, data obtained by using LES (Kassera *et al.* 1995) are compared with the current k–ω-based simulation results.

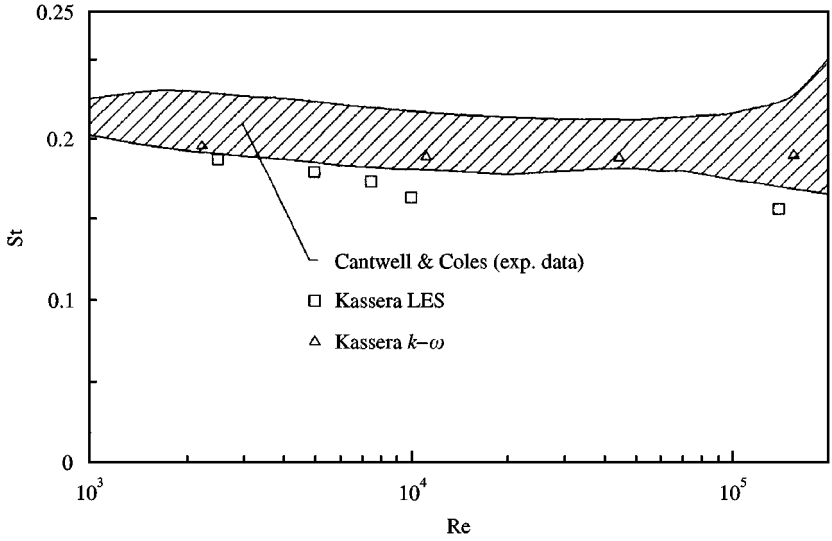

Figure 7. Strouhal numbers of a single fixed tube.

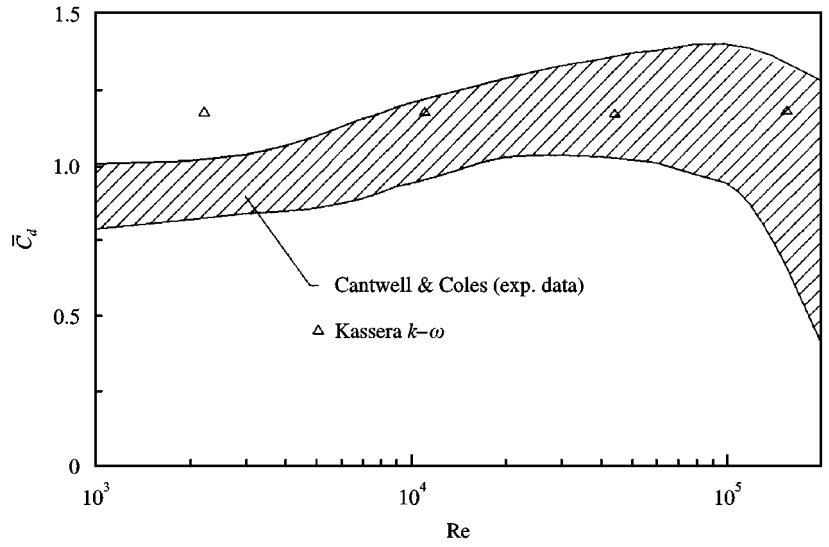

Figure 8. Drag coefficient of a single fixed tube.

4.2. Tube Bundles with High Pitch-to-Diameter Ratios

Simulation of tube-bundle vibrations was done by modelling the tube bundle in a channel flow, the configuration used in the experimental investigations (Figure 3). For comparison, a r.m.s. amplitude has been utilized in the following manner:

$$A_{\mathrm{rms}} = \frac{\sqrt{\Delta x_{\mathrm{rms}}^2 + \Delta y_{\mathrm{rms}}^2}\,100}{D} \tag{16}$$

in percent of the diameter. The experimental raw data were obtained by measuring tube vibrations at a constant approach velocity over 2 s with a sample rate of 250 Hz. Numerical data were produced by simulating tube-bundle vibrations until they became quasi-steady. From this point onwards, about 20 additional cycles were calculated and evaluated by equation (16). Figures 9 and 10 depict the increase of the amplitues A_{rms} of the middle measuring tube (marked) with the increase of the approach velocity u_0. Twelve velocity

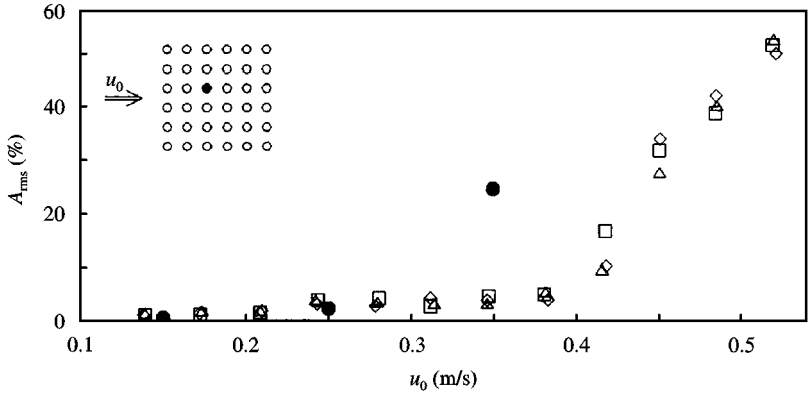

Figure 9. Tip amplitudes of bundle 03: □, experimental data first repetition; ◇, experimental data second repetition; △, experimental data third repetition; ●, simulation.

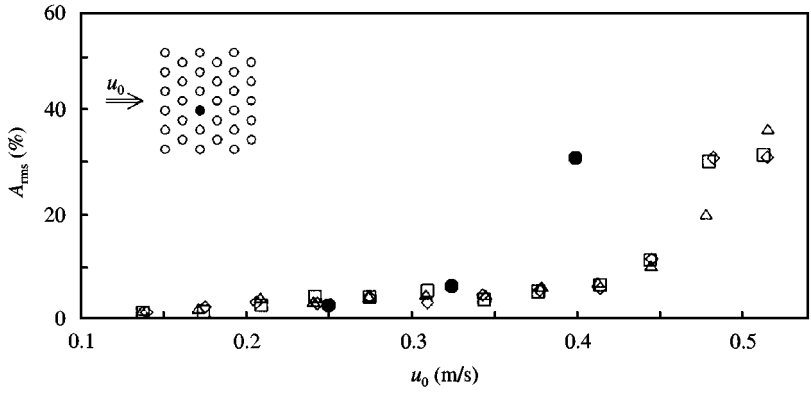

Figure 10. Tip amplitudes of bundle 12: □, experimental data first repetition; ◇, experimental data second repetition; △, experimental data third repetition; ●, simulation.

steps were considered in the experimental investigations; each of them was repeated three times. Simulation was carried out at three approach velocities. At the first two velocity steps, the calculated tube amplitudes fit very well with the experimental data. At the third velocity step, the amplitude is overestimated significantly. At all approach velocities, the transverse tube amplitude is dominant over the tube amplitude in the x-direction for both the simulation and the experimental data.

If Fast-Fourier-Transform analysis is applied on the cross-stream tube motion data, two significant peaks appear in the frequency spectrum. The first peak corresponds to vortex shedding, and the second to the natural frequency of the tube in the bundle. To obtain a dimensionless description, two reduced frequencies are defined with these frequencies (based on the gap velocity) and plotted versus the approach velocity, as shown in Figure 11 [for details see Kassera & Strohmeier (1994)]. Again, there are 12 velocity steps of the experimental investigations for each simulated tube bundle. The straight line represents the oscillating fluid forces and the parabolic curves are the constant natural frequencies of the tubes. It can be seen that the natural frequency (in flow) is reproduced very well by the calculation scheme, although the added mass is not an input parameter but is simulated implicitly. In addition, the vortex-shedding frequency agrees with experimental data. At the third velocity step of the simulations, it can be observed that there is only one frequency peak in the spectrum; the vortex-shedding frequency has switched to the natural frequency (Figure 11). This causes the significant overestimation of the simulated amplitudes at higher velocities.

The scattering of the vortex-shedding-based reduced frequency of the staggered bundle 12 is probably caused by the limited size of the vortices in that case. Figures 12 and 13 show the flow patterns, and it is obvious that the vortices in bundle 12 are more suppressed and irregular.

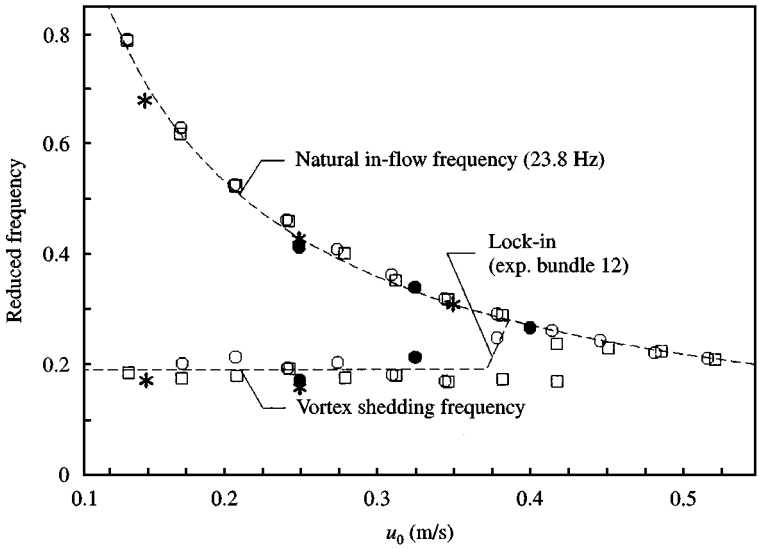

Figure 11. Reduced frequency versus approach velocity: □, bundle 03 experimental data; ∗, bundle 03 simulation; ○, bundle 12 experimental data; ●, bundle 12 simulation.

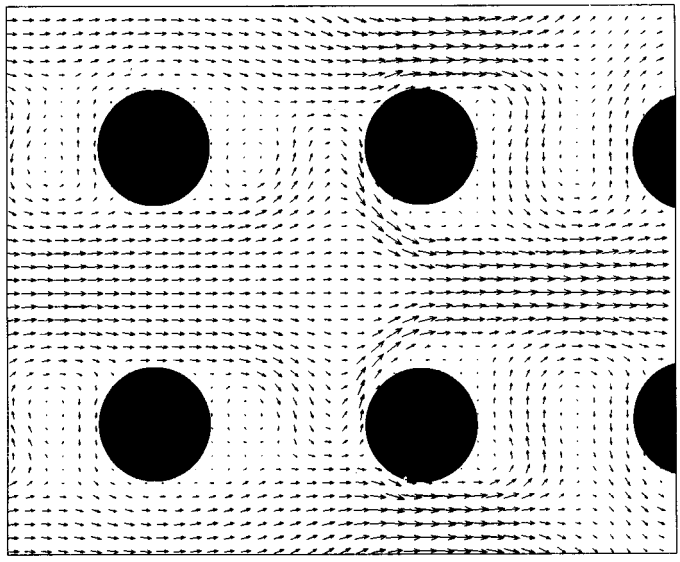

Figure 12. Bundle 03: flow pattern at $u = 0{\cdot}25$ m/s.

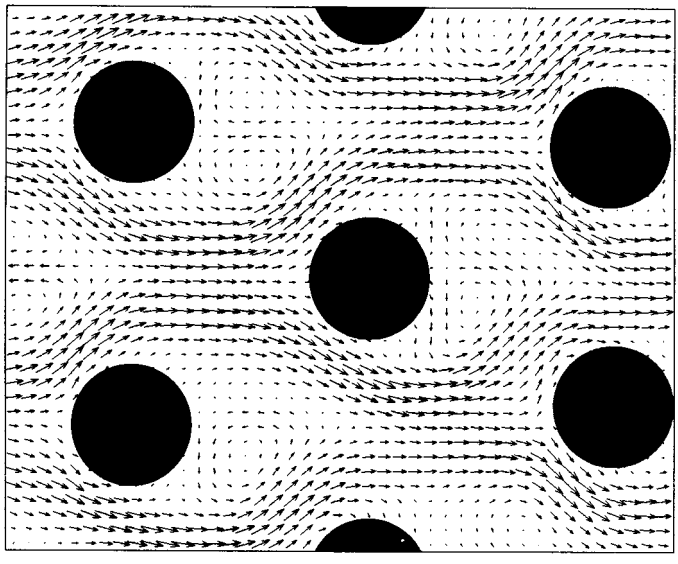

Figure 13. Bundle 12: flow pattern at $u = 0{\cdot}325$ m/s.

Compared with other experimental data, the Strouhal numbers of about 0·19 are too low. Polak & Weaver (1994), for example, suggested for normal triangular arrays the equation

$$\mathrm{St} = \frac{P/D - 1}{P/D} \frac{1}{1{\cdot}73(P/D - 1)} \tag{17}$$

for $P/D \geq 2{\cdot}0$, which leads in the case of the bundles 03 and 12 to St = 0·24. Fitz-Hugh (1980) gives St = 0·21 for the in-line array and St = 0·25 for the staggered array. One reason for this deviation may be that the frequencies are measured on the vibrating tubes, while Polak & Weaver are measuring in nonvibrating tube bundles. They report also that there are some data of Pettigrew & Gorman (1978) which are substantially below the rest of the data. These data were also obtained from large-amplitude tube response in water flow. In the investigations presented here, however, both simulation data and experimental data were obtained and evaluated by the same procedures, and the frequencies correspond well. Therefore, it can be concluded that the Strouhal numbers predicted by the calculation scheme agree reasonably well with experimental data.

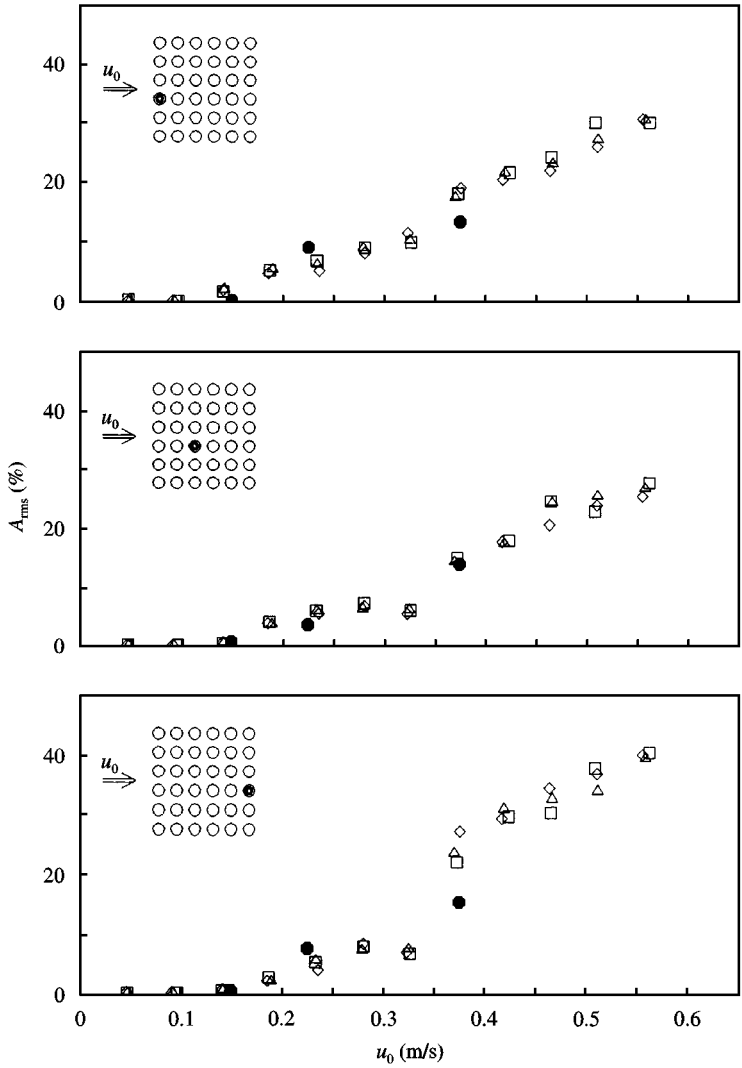

Figure 14. Tip amplitudes of bundle 05: □, experimental data first repetition; ◇, experimental data second repetition; △, experimental data third repetition; ●, simulation.

4.3. Medium and Low Pitch-to-Diameter Ratios

In the bundles investigated with medium and low P/D, vortex shedding is suppressed due to the smaller gaps between the tubes. Therefore, other mechanisms like fluid elastic instabilities become dominant.

The comparison with experimental data is given in Figures 14–17. There, the calculated amplitudes are plotted for all measuring tubes (marked in the outline of the bundle). The following should be noted.

(i) Again, as for the bundles with high P/D, the main contribution to the total amplitude A_{rms} is made by the cross-stream amplitude Δy_{rms}.

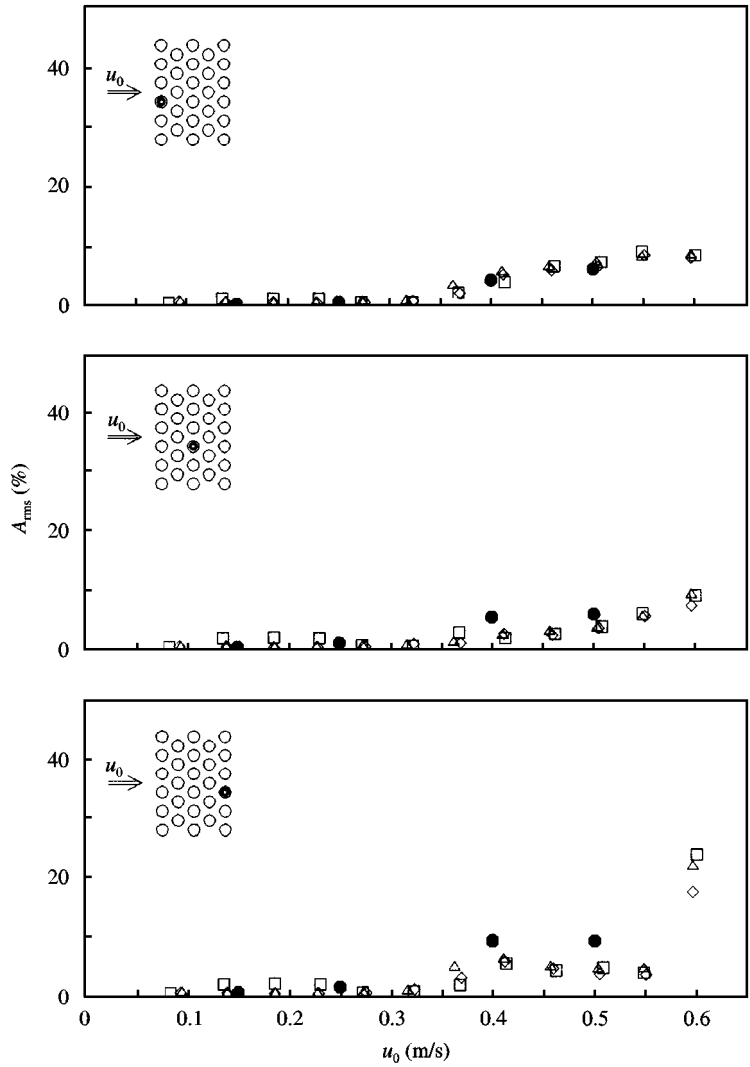

Figure 15. Tip amplitudes of bundle 14: □, experimental data first repetition; ◇, experimental data second repetition; △, experimental data third repetition; ●, simulation.

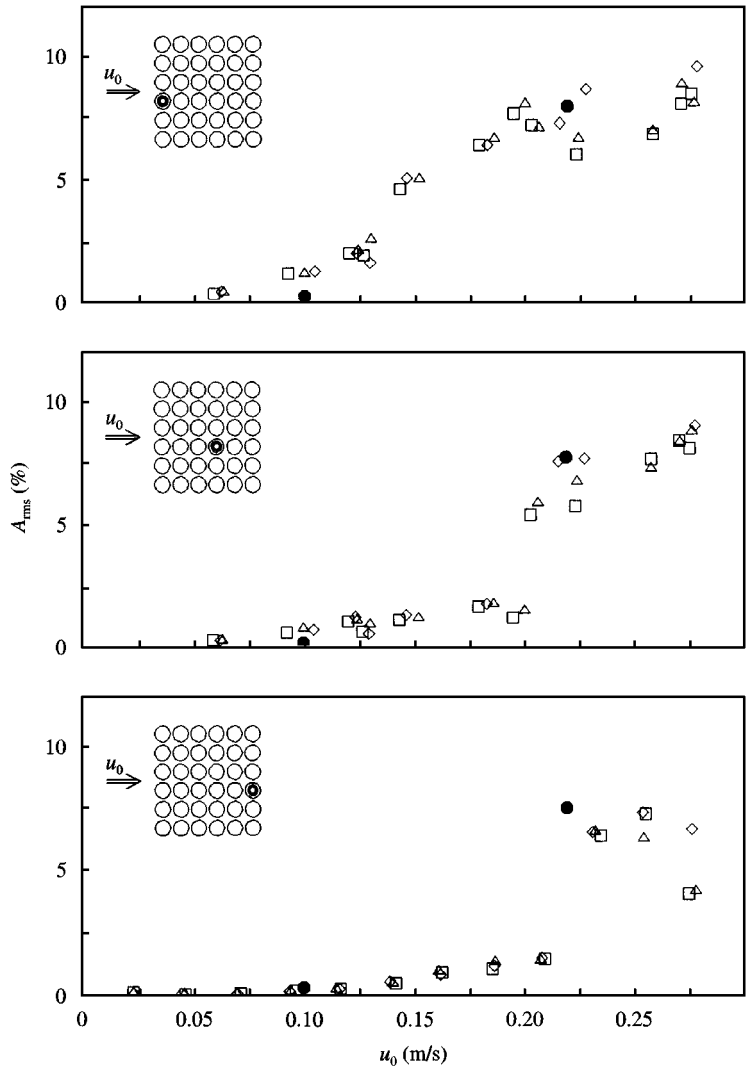

Figure 16. Tip amplitudes of bundle 07: □, experimental data first repetition; ◇, experimental data second repetition; △, experimental data third repetition; ●, simulation.

(ii) The last row of bundle 05 becomes unstable at $u_0 \approx 0.35$ m/s. The amplitudes of the simulation point at $u_0 = 0{\cdot}375$ m/s are smaller than the measured amplitudes. This is caused by a tube-displacement limitation in the calculation scheme, which was employed to avoid numerical instabilities. Calculating the point of instability with the criterion suggested by Pettigrew & Taylor (1991),

$$u_{r,\mathrm{crit,th}} = 3{\cdot}0\delta_r^{0{\cdot}5}, \tag{18}$$

a critical approach velocity of $u_{0,\mathrm{crit,th}} = 0{\cdot}15$ m/s is obtained (Table 1).

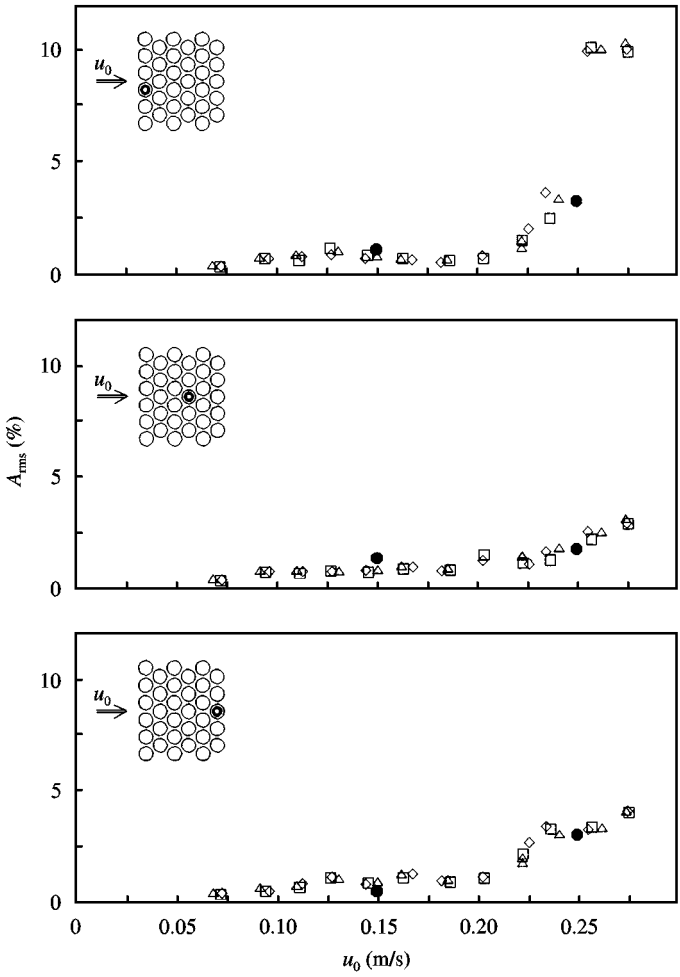

Figure 17. Tip amplitudes of bundle 16: □, experimental data first repetition; ◇, experimental data second repetition; △, experimental data third repetition; ●, simulation.

(ii) In the case of bundle 14, only sub-critical velocities were simulated. In the experiment, the last row became unstable at the 12th velocity point. The instability threshold is $u_{0,\mathrm{crit,exp}} \approx 0{\cdot}57$ m/s. Comparing the experimental amplitudes with the computed ones, it can be stated that the correspondence is quite good, with the exception of those of the last tube row where the predicted amplitudes are too large. Equation (18) predicts a critical approach velocity of $u_{0,\mathrm{crit,th}} = 0{\cdot}26$ m/s, less than the half of the real value.

(iv) On bundles 07 and 16, the predicted amplitudes of the tubes are within the scatter of the experimental data in both cases. Calculating the instability threshold with equation (18) leads to $u_{0,\mathrm{crit,th}} = 0{\cdot}10$ m/s, while the values obtained by experiments are $u_{0,\mathrm{crit,exp}} = 0{\cdot}20$ m/s for bundle 07 and $u_{0,\mathrm{crit,exp}} = 0{\cdot}23$ m/s for bundle 16.

5. CONCLUSIONS

Flow-induced vibrations of six different tube bundles have been predicted with a numerical calculation scheme†. For the bundles with medium and low P/D, the computed amplitudes agree well with experimental data in general. Regarding the two bundles with high P/D, this statement is valid for low and medium approach velocities only. Lock-in is predicted too early, probably because of the restriction of the calculation scheme to two dimensions. Therefore, the vortices are treated as fully correlated over the whole tube length, an assumption which is not valid in real tube bundles.

Compared with the conventional methods of predicting vibration behaviour, the simulation has the following advantages: (a) prediction of the amplitudes of all tubes at any desired velocity; (b) all the mechanics of fluid elastic instability are provided, the flow field is available at every location in the computational domain at every time, as well as the dynamical data of all tubes; (c) more flexibility when calculating irregular arrangements.

Furthermore, with increasing computer power it seems to be possible to simulate tube-bundle vibrations with three-dimensional models. Then, the uncertain application of methods obtained by two-dimensional analysis for the prediction of stability of three-dimensional heat-exchanger spans subjected to nonuniform flow will no longer be necessary.

REFERENCES

AU-YANG, M. K., BLEVINS, R. D. & MULCAHY, T. M. 1991 Flow induced vibration analysis of tube bundles—a proposed section III appendix N nonmandatory code. *ASME Journal of Pressure Vessel Technology* **113,** 257–267.

BLEVINS, R. D. 1990 *Flow-Induced Vibration.* New York: Van Nostrand Reinhold.

CANTWELL, B. & COLES, D. 1983 An experimental study of entrainment and transport in the turbulent near wake of a circular cylinder. *Journal of Fluid Mechanics* **136,** 321–374.

FITZ-HUGH, J. S. 1973 Flow-induced vibration in heat exchangers. In *Proceedings of the International Symposium on Vibration Problems in Industry*, Keswick, U.K., paper 427.

FRANKE, R. 1991 Numerische Berechung der instationären Wirbelablösung hinter zylindrischen Körpern (Numerical calculation of the vortex shedding behind cylindrical bodies). Ph.D. dissertation, Technical University of Karlsruhe, Germany.

ICHIOKA, T., KAWATA, Y., IZUMI, H., NAKAMURA, T. & FUJITA, K. 1994 Two-dimensional flow analysis of fluid structure interaction around a cylinder and a row of cylinders. In *Proceedings ASME Symposium on Flow-Induced Vibration* (ed. M. K. Au-Yang), PVP-Vol. 273, pp. 33–41. New York: ASME.

ICHIOKA, T., KAWATA, H., IZUMI, H., NAKAMURA, T. & TAKAMATSU, H. 1995 Two-dimensional analysis of fluid–structure interaction around a tube row and a tube array in cross-flow. In *Proceedings Third International Conference on Nuclear Engineering* (ICONE-3), Kyoto, Japan, Vol. S125-2, pp. 603–608.

KASSERA, V., KACEM-HAMOUDA, L. & STROHMEIER, K. 1995 Numerical simulation of flow induced vibration of a tube bundle in uniform cross-flow. In *Proceedings ASME Symposium on Flow-Induced Vibration* (ed. M. J. Pettigrew), PVP-Vol. 298, pp. 37–43. New York: ASME.

KASSERA, V. & STROHMEIER, K. 1994 Experimental determination of tube bundle vibrations induced by cross-flow. In *Proceedings ASME Symposium on Flow-Induced Vibration* (ed. M. K Au-Yang), PVP-Vol. 273, pp. 91–97. New York: ASME.

† All computations were carried out on a CRAY YMP. The average CPU time needed for one velocity point was about 12 h.

LEONARD, B. P. 1979 A stable and accurate convective modelling procedure based on quadratic interpolation. *Computer Methods in Applied Mechanics and Engineering* **19,** 59–98.
PATANKAR, S. V. 1980 *Numerical Heat Transfer and Fluid Flow*. New York: Hemisphere.
PETTIGREW, M. J. & TAYLOR, C. E. 1991 Fluidelastic instability of heat exchanger tube bundles: review and design recommendations. *ASME Journal of Pressure Vessel Technology* **113,** 242–256.
POLAK, D. R. & WEAVER, D. S. 1994 Vortex shedding in normal triangular tube arrays. In *Proceedings ASME Symposium on Flow-Induced Vibration* (ed. M. K. Au-Yang), PVP-Vol. 273, pp. 145–156. New York: ASME.
PRICE, S. J. 1995 A review of theoretical models for fluidelastic instability of cylinder arrays in cross-flow. *Journal of Fluids and Structures* **9,** 463–518.
SADAOKA, N. & UMEGAKI, K. 1995 Analysis of vortex-induced vibration in an array of tubes. In *Proceedings ASME Symposium on Flow-Induced Vibration* (ed. M. J. Pettigrew), PVP-Vol. 298, pp. 29–36. New York: ASME.
WILCOX, D. C. 1994 *Turbulence Modelling for CFD*. La Cañada, CA: DCW Industries Inc.

APPENDIX: NOMENCLATURE

A_{rms}	r.m.s. amplitude of a tube, equation (16)
c	elastic spring constant
C_d	mean drag coefficient
D	outer tube diameter
F_y	sum of all transverse fluid forces acting on a special tube
f_n	tube natural frequency in still water
f_r	reduced frequency, $(fD)/u_{\text{gap}}$
f_v	vortex separation frequency
k	kinetic energy of turbulent fluctuations per unit mass
m_a	added mass per unit length
m_c	contained mass per unit length
m_s	structural mass per unit length
n_{it}	maximum number of iteration sweeps per time step
p	pressure
P/D	pitch-to-diameter ratio
Re	Reynolds number $(u_{\text{gap}}D)/v_f$
St	Strouhal number, f_vD/u_{gap}
t	time
Δt	time increment
u	streamwise velocity component
u_0	approach velocity
$u_{0,\text{crit,exp}}$	critical approach velocity obtained by experiments
$u_{0,\text{crit,th}}$	critical approach velocity obtained by equation (14)
u_{gap}	gap velocity, $u_0(P/D)/[(P/D) - 1]$
u_r	reduced velocity, $u_{\text{gap}}/(f_nD)$
$u_{0,\text{crit,exp}}$	critical reduced velocity obtained by experiments
$u_{0,\text{crit,th}}$	critical reduced velocity obtained by equation (14)
v	transverse velocity component
x	streamwise coordinate
Δx	tube displacement in the x-direction
Δx_{bg}	average spacing of the base grid
Δx_{tg}	average spacing of the tube grids
$\dot{x}$	tube velocity in the x-direction
$\ddot{x}$	tube acceleration in the x-direction
y	transverse coordinate
Δy	tube displacement in the y-direction
$\dot{y}$	tube velocity in the y-direction
$\ddot{y}$	tube acceleration in the y-direction

δ_r	reduced mass-damping, $(2\pi m\zeta)/(\rho D^2)$
ζ	damping factor; $2\pi\zeta = \log.$ decrement
v	kinematic viscosity
v_f	kinematic viscosity of cross-flow medium
v_t	local turbulent viscosity
ρ	density of cross-flow
ω	specific dissipation rate